Mutual interference of layer plane and natural fracture in the failure behavior of shale and the mechanism investigation – A numerical study

Peng Zhao[1,2], Lingzhi Xie[1,3], Zhichao Fan[2], Kun Liang[2], Lei Deng[2], Jun Liu[1,3,*]

[1] National Key Laboratory of Hydraulics and Mountain River Engineering, Sichuan University, Chengdu 610065, China.

[2] College of Architecture and Environment, Sichuan University, Chengdu 610065, China.

[3] Institute of New Energy and Low-carbon Technology, Sichuan University, Chengdu 610065, China.

Corresponding author: J. Liu (j.liu@scu.edu.cn)

Key Points:

- PFC-based numerical model are conducted to simulate the failure behavior of layered shale with natural fracture under Brazilian tests.
- Complex interference of layer plane and natural fracture in failure strength and fracture pattern of shale are clarified.
- Damage modes, micro cracks and sensitivity of tensile/cohesion strength are recognized quantitatively during loading/failure process.

Abstract

Shale contains a certain amount of natural fractures, which affects the mechanical properties of shale. In spite that significant progress has been made, how natural fractures interfere the failure behaviour of layered shale remains unclear and need to be examined. In this paper, a bonded-particle model in particle flow code (PFC) is established to simulate the failure process of layered shale under Brazilian tests, under the complex relationship of layer plane and natural fracture. First, a shale model without natural fractures is verified against the experimental results. Simultaneously, the impact of the layer plane angle (marked as α) on the failure process in intact shale is exposed. Then, a natural fracture is embedded in the shale model, where the outcomes indicate that α and the angle (marked as β) of embedded fracture prominently interfere the failure strength anisotropy and fracture pattern. Finally, sensitivity evaluations suggest that variable tensile/cohesion strength has a changeable influence on failure mechanism of shale, even for same α or/and β. To serve this work, the stimulated fractures are innovatively and concisely categorized into two patterns based on whether they relate to natural fracture or not. Meanwhile, four damage modes (matrix shear, matrix tension, layer shear and layer tension) and the number of micro cracks during the loading process are recognized quantitatively to study the mechanism of shale failure behaviour. Considering the failure mechanism determines the outcome of hydraulic fracturing in shale, this work is supposed to provide a significant implication in theory for the engineering operation.

Plain Language Summary

Either layer plane or natural fracture has significant influence on shale failure behavior - let alone their complex combination. Unfortunately, the mutual interference of layer plane and natural fracture in the failure behavior of shale keeps unclear and need to be excavated. In this study, the failure strength, fracture pattern, damage mode and sensitivity of tensile/cohesion strength are recognized quantitatively during the loading process, based on a series of PFC-based numerical simulations under Brazilian tests. This study made a systematically and profoundly description on the failure behavior of layered shale containing natural fracture, in which some viewpoints are rarely exposed in existing achievements. This work is supposed to be a significant implication to the field engineering operation in theory.

1 Introduction

Hydraulic fracturing is an effective technique to stimulate shale gas reservoirs, which enables the boom of shale gas development over the world (Li et al., 2018; Wanniarachchi et al., 2018; Mohtar et al., 2019; Yin et al., 2017; Zhou et al., 2019). Shale is usually characterized as layered and contains complex natural fractures (Liu et al., 2016; Liu et al., 2017). Previous achievements noted that these discontinues make the mechanical properties of shale more complex, resulted in that the failure patterns of shale mainly depend on the mechanical characteristics of the layer planes and natural fractures as well as the relationship between them (e.g., März et al., 2008; Vervoort et al., 2014; Tan et al., 2015). Therefore, there is a strong need to better understand the mechanical characteristics and failure process of shale regarding fracturing engineering applications.

Because natural fracture is variable to shale with a different geological background (e.g., sedimentary or structural environment), it is challenging to universally describe the failure mechanisms of shale containing natural fracture in theory. To address this issue, rock mechanics

methods like Brazilian tests, compression tests and notched three-point-bending tests were conducted in laboratory to investigate the failure behaviour of rocks with flaws, in which these flaws simulate natural fractures (Alm et al., 1985; Planas et al., 1999; Na et al., 2017; Feng et al., 2019). For example, Yang et al. (2015), Zhang et al. (2018) and Nezhad et al. (2018) experimentally studied the effect of the layer-loading angle on the failure mode of Brazilian tests. Heng et al. (2015) conducted direct shear tests to study the mechanical properties of layer planes and the shear strength of shale with different layer orientations. More examples like Arora et al. (2015), Geng et al. (2016) and Al-Maamori et al. (2019) made triaxial compression tests on shale to analyze the variation law of transversely isotropic elastic parameters, aiming to obtain the relationship between the elastic parameters and layer angle. Shi et al. (2019) conducted notched three-point bending tests to elucidate the fracture behaviour of anisotropic shale. By experimental studies, these above researches accumulated a lot of knowledge about mechanical characteristic of shale. However, in laboratory, it is not easy to prepare shale samples containing flaws (pre-existing fracture) with variable characteristics (e.g., width, length, intersection angle with layer plane, etc.). This shortage of experimental attempts limits researchers to systematically interpret the failure property of layered shale with natural fracture, resulted in the effect of natural fracture on the shale failure behaviour remains unclear and need to be examined.

As an alternative research method, numerical simulation can be regarded as a supplement to the experiments, since it is able to easily control the variables and gather more operating conditions in a model. According to different means of describing weak planes, existing numerical methods are divided into continuous medium methods (CMMs) and discrete element methods (DEMs). In contrast to the CMM (Cai, 2013; Zeng and Wei, 2016), DEM procedure is able to intuitively embody the weak planes, where the initiation and propagation of fractures can be obtained explicitly without applying complex constitutive laws (Bennett et al., 2015; Park and Min, 2015; Wang et al, 2018; Zhang et al., 2018; Zhang et al., 2019). In addition, considering the small scale (e.g., diameter of 50 mm) of the specimens, the particle DEM, e.g., particle flow code (PFC), is widely used to describe the gradual failure of rocks and the microscopic mechanisms underlying rock deformation behaviour (Zhou et al., 2016; Jia et al., 2017). Hence the PFC is widely introduced to the numerical simulation about shale issues. For example, He et al. (2018) investigated the influence of the shale layer plane orientation and layer cohesion on the tensile strength and fracture modes under Brazilian tests. Chong et al. (2017) proposed an anisotropic mineral brittleness-based model to study shale properties and found that the ratio of cohesion to tensile strength of smooth joints mainly affects the number of cracks formed. Besides, Yang and Huang (2014), Luo et al. (2018) and Dou et al. (2019) also numerically studied the mechanic behaviour using PFC. Unfortunately, in spite that numerical investigations were conducted extensively, of which sparing PFC-based ones have went to the failure performance of shale containing natural fracture.

In this study, a DEM-based numerical model is established for Brazilian tests. Based on PFC2D, the established layered shale model without fractures (referred to as intact shale) is first validated against laboratory results. Then, a single flaw is embedded into the intact model to simulate the failure behaviour of shale with natural fracture. Finally, this work further discusses the sensitivity of layer plane strength parameters (namely, tensile/cohesion strength) on the failure strength and fracture pattern of shale containing natural fracture. During the investigation, this work puts forward a novel and concise classification scheme on the fractures stimulated by Brazilian tests. Moreover, this work quantitatively identifies the damage modes (matrix shear, matrix tension, layer shear and layer tension) and the number of micro cracks during the loading

process, aiming to expose the mechanism of shale failure behaviour. Basically, this study focuses on the interference of different discontinuities (natural fracture and layer plane) on the failure behaviour of shale, which is expected to be helpful in guiding field engineering operation of hydraulic fracture theoretically.

2 Numerical model establishment and validation

An intact shale model is built for the numerical model validation by compared with the experimental investigation using the Brazilian disk test. This model has a disk shape with a diameter of 50 mm, which is the same as the experimental disks. According to the sensitivity analysis of numerical parameters (Ding et al., 2014), reasonable results can be obtained when the model size is 50 times larger than the average particle radius and the particle radius ratio is close to 1.66. Moreover, shale comprises a series of thin layer planes, and the spacing between the layers generally varies from 0.1 mm to 1 mm (Zhang et al., 2017). To ensure the efficiency of the calculation and the accuracy of the results, the distance between the layers of the numerical model is set to 1 mm. The total number of particles is 14661, with a uniform distribution of particle sizes ranging from 0.15 mm to 0.25 mm. The flat joint model (FJM) and the smooth joint model (SJM) are used to simulate shale matrix and layer planes, respectively. The details of these two models are exhibited by Wang et al. (2014) and Wu et al. (2018).

2.1 Calibration for the micro-parameters of the intact shale model

As for the PFC2D model, it is difficult to directly obtain the micro-parameters of the particles and the contacts through experimental results. The most common method to determine these micro-parameters is transformed from the macroscopic mechanical properties of samples *via* trial-and-error approach (e.g., Luo et al., 2018). Accordingly, the micro-parameters of the intact shale model are corrected (Table 1), based on the comparison between load-displacement curves, failure strength and fracture patterns.

In the numerical simulation, the vertical displacement of the load plate is related to the loading time. It should be noted that the loading rate in the numerical model is different from that in the experiment. The PFC simulation uses displacement loading with a loading rate of 0.2 m/s, which tends to be converted to 3.6×10^{-9} m/step when the time step is set to 1.8×10^{-8} s/step. That is, the load plate moving 1 mm requires approximately 277777 steps. Therefore, 0.2 m/s is slow enough to simulate quasi-static loading (Gao et al., 2016).

Table 1. Micro-parameters of the intact shale model

Model types	Micro-parameters	Values
Flat joint model (FJM)	Young's modulus of the particle (GPa)	20
	Particle radius (mm)	0.15~0.25
	Porosity	0.05
	Ratio of the normal to shear stiffness	1.6
	Tensile strength (MPa)	12
	Cohesion (MPa)	60
	Friction coefficient	0.5
	Friction angle (°)	30
Smooth joint model (SJM)	Normal stiffness (GPa/m)	10000
	Shear stiffness (GPa/m)	2000
	Tensile strength (MPa)	4
	Cohesion strength (MPa)	15
	Friction coefficient	0
	Friction angle (°)	70

2.2 Comparison of the numerical and experimental results for intact shale

The testing samples were taken from fresh outcrops of the Silurian Longmaxi formation. To consider the influence of the layer angle on the failure strength, the layer angle (α) is defined as the angle between the loading direction and the normal direction of the layer plane (Fig. 1). For the purpose of numerical model validation, seven layer angles (0°, 15°, 30°, 45°, 60°, 75° and 90°) are adopted in the experimental tests. The tensile strength of intact shale is estimated by the maximum load measured in the Brazilian splitting test using sample with standard size (thickness of 25 mm and diameter of 50 mm). Once the peak load is measured in the experiment, the tensile strength can be calculated as:

$$\sigma_t = \frac{2F}{\pi D t} \qquad (1)$$

where F is the peak load; D and t are the diameter and thickness of the sample, respectively.

It should be noted that the tensile strength calculated from Eq. (1) is appropriate for the homogeneous isotropic rocks with fracture initiating from the centre of specimen. However, shale is generally characterized as heterogeneous, where the failure is not restricted to tensile damage in specimen centre for most cases. Therefore, as for the Brazilian tests of shale, the value based on Eq. (1) is usually described as the failure strength, aiming to normalize the load to the diameter and thickness (Xu et al., 2018).

The load-displacement curves during Brazilian tests of the numerical and experimental performances are presented in the Fig. S1 of Supporting Information (SI). The results show that the load-displacement curves calculated from the model are in good agreement with the experimental datas. In addition, after the peak is reached, both the numerical and experimental load-displacement curves drop rapidly, indicating that the shale samples have failed.

The comparison of investigations obtained from the experiments and numerical simulation methods indicates the failure strength is anisotropic and decreases with increasing α (Fig. 2). Moreover, Fig. 2 also demonstrates the failure strength from the two methods is consistent at different α. With regard to the fracture patterns of the shale samples, the two methods also show good agreement (Figs. S2 and S3). Referring to Figs. S2 and S3, the fracture pattern of shale with low α (0° and 15°) can be regarded as a straight-line failure, where the damage mainly occurs in the matrix. As the α increases (30° and 45°), the fracture pattern changes from straight-line failure to curve-line failure. When the α increases to 60° and 75°, part of the damage develops along the layer. Finally, when the α is 90°, the damage is the pattern of straight-line failure again, in which the specimen is destroyed along the layer plane.

In conclusion, the displacement-load curve, failure strength and fracture pattern are comprehensively compared between numerical and experimental methods. Based on the good agreements above, the numerical method with the parameters of intact shale are feasible.

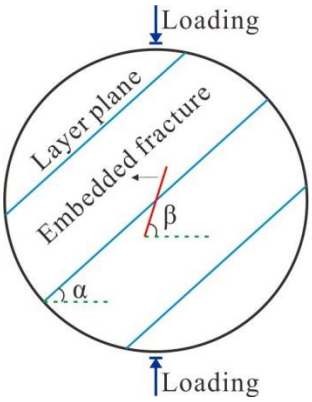

Figure 1. Schematic view for the definition of layer angle (α) and fracture angle (β)

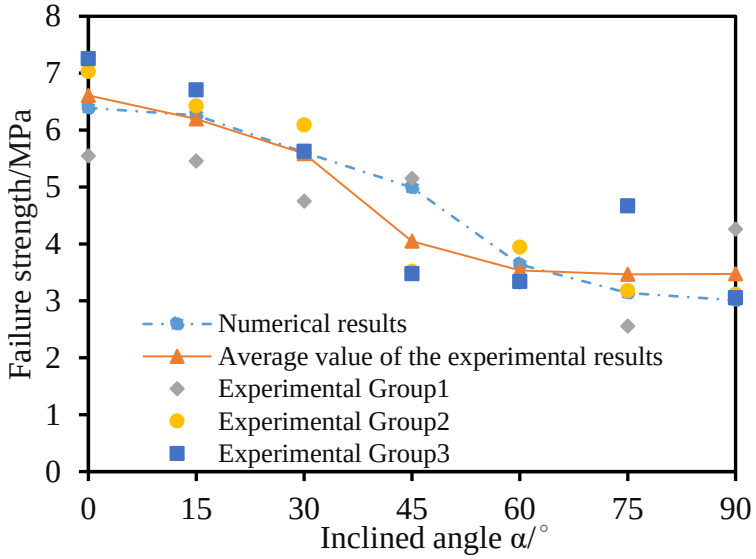

Figure 2. Variation in failure strength with different α during experimental and numerical operations

2.3 Evolution of micro cracks in intact shale

The process of deformation and destruction are often accompanied by the absorption, accumulation and dissipation of energy (Zhao et al., 2008). This part mainly studies the influence of the layer angle α on the absorption energy and the damage evolution during the loading process and further reveals the mechanical characteristics of shale.

Here, the absorption energy is the energy exerted by the external force and is calculated as the area enclosed by the load-displacement curve and the abscissa axis. The absorption energy curves of intact shale with different α are plotted in Fig. 3. In this figure, the axial displacement ratio is defined as the ratio of the loading displacement to the displacement in the peak of loading force. It can be seen that the absorption energy evolution curve grows nonlinearly. The growth rate of adsorption energy is small in the initial stage for different α, corresponding to the compaction phase of the samples. Then, the growth rate gradually increases due to the occurrence of micro cracks. When the axial displacement ratio is 80% ~ 90%, the growth rate of energy adsorption is essentially stable (revealed by the slope of curves in Fig. 3). Besides, the distinctions among samples indicate that α has a significant influence on the absorption energy,

where the sample with lower α tends to absorb more energy with a higher growth rate. Previous viewpoints suggest that the growth rate of absorption energy reflects the severity of shale failure (Zhang et al., 2018), which keeps consistent with damage mechanisms of shale plotted in Fig. 4. The shale with lower α contains a dominant proportion (and a higher quantity) of micro cracks in shale matrix and thus involves a greater growth rate of absorption energy, while that with higher α has an inferior proportion (and a lower quantity) of micro cracks in the matrix and thus corresponds with a lower growth rate of absorption energy (Figs. 3, 4 and 5).

The damage occurring inside the shale samples can be characterized by the evolution of micro cracks during the loading process, of which the entire shale failure process can be divided into three stages, as shown in Fig. 5.In the OA stage, there are no micro cracks generated in the samples for all α, in which point O is the starting point of loading. The micro pores inside the shale elastically deform and gradually close under compression. At this time, the absorption energy is converted into the elastic potential energy of the shale sample. When the displacement is loaded to point A, micro cracks begin to appear (Fig. 5). During the AB stage, part of the absorption energy is converted into elastic potential energy, and the rest is released in the form of damage. Hence, the sample can still bear a load, and the rate of energy growth increases steadily (Fig. 3). In AB phase, the α has an effect on the increasing characteristics of the micro crack extent, where the development of micro cracks is describes as three manners. Firstly, when the α is low (0° and 15°), the matrix damage determines the failure of shale samples and appears as a straight-line type. Here, the evolution characteristic shows an "incremental" mode, where the growth rate of the crack number increases gradually (Fig. 5a). Secondly, layer damage tends to occur with increasing α (30°~60°), while the matrix damage still plays a dominant role. The straight-line type of failure changes to the curve-line type. In this condition, the evolution of micro cracks is a "smooth" mode and rises slowly at a fixed rate (Fig. 5b). Thirdly, when the α increases to 75° and 90°, the layer damage leads to the failure of the shale samples. This evolution characteristic is described as a "stepped" mode, indicating that micro cracks develop quickly in a period of time and then remain undeveloped, with repeats for several times (Fig. 5c). With regard to the BC stage, the damage develops unstably with a rapid increase of micro cracks for all α (Fig. 5), in which the absorption energy and the released energy reach a relatively balanced state until the sample has completely failed. In addition, the source of micro cracks (tensile or shear) in Fig. 5 keeps pace with that shown in Fig. 4, further suggesting that the fracture patterns and failure mechanisms determine the evolution of the micro cracks (that is, the damage process).

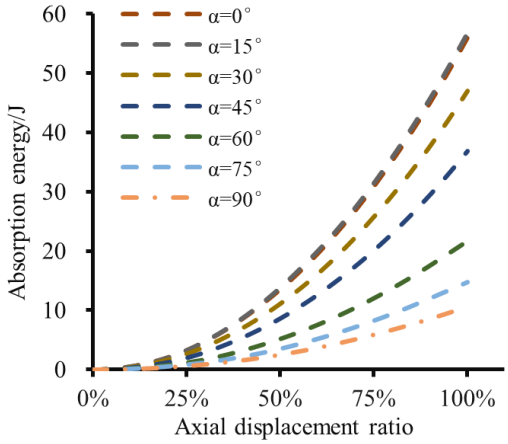

Figure 3. Energy absorption curves of intact shale during loading process

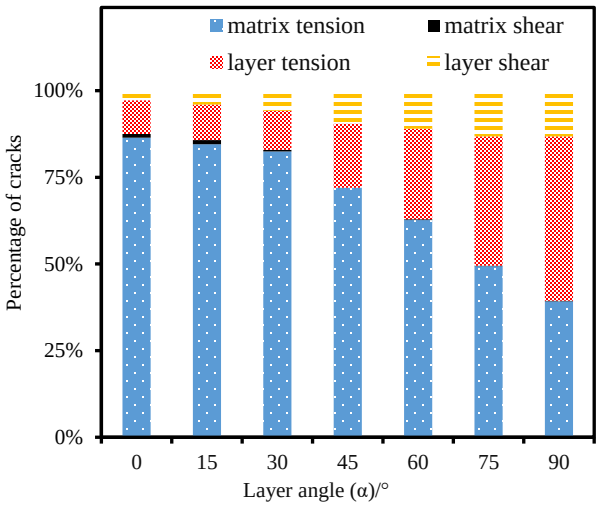

Figure 4. Micro cracks from different damage mechanisms of intact shale

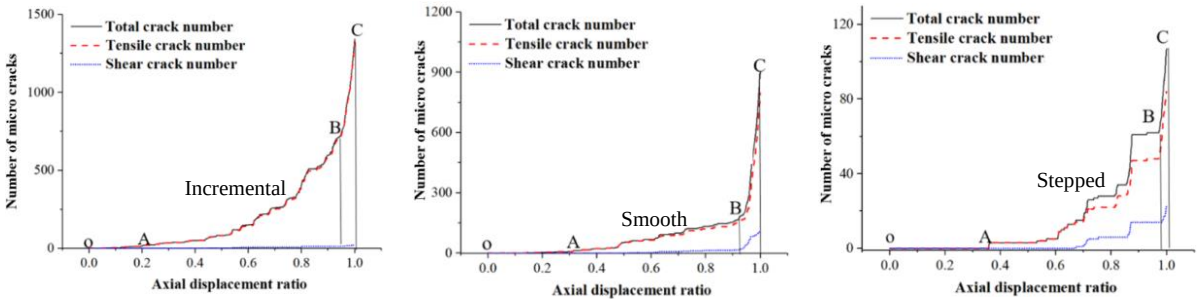

(a) α=0° (b) α=45° (c) α=90°

Figure 5. Evolution of micro cracks of intact shale at different α

3 Numerical model of shale embedded with fracture

According to the simulation of intact shale discussed above, the numerical approach is reliable to assess the fracture behaviour of shale under Brazilian tests, in that the numerical results are in good agreement with the experimental ones. On this basis, a single fracture is embedded in the centre of the specimen to study the mechanical properties of shale with natural fracture under the conditions of Brazil test. The ratio of the embedded fracture length to the sample radius is 0.3 that keeps same with some existing experimental operations and is wide adopted in numerical simulations of Brazilian tests (e.g., Haeri et al., 2014; Zhou et al., 2016).

In this section, the influence of the relative position relationship between the fracture and layer is mainly considered, where the definition of fracture angle (β) is shown in Fig. 1. Here both α and β have seven different angles (0°, 15°, 30°, 45°, 60°, 75° and 90°) for the numerical calculation. On the basis of SJM model, the embedded fracture is simulated with the microscopic parameters referred from Zhou et al. (2017), with a normal stiffness of 3000 GPa/m, a shear stiffness of 500 GPa/m, a tensile strength of 0.05 MPa, a cohesion strength of 0.05 MPa, and a friction angle of 31°.

3.1 Influence from α and β on the failure strength

It can be seen that the failure strength of shale embedded with fracture exhibits anisotropy (Fig. 6a). When β remains unchanged, the failure strength decreases along with the increasing α, which is similar with the behaviour of intact shale. According to Fig. 6a, for different β, the failure strength anisotropy of shale shows different characteristics with the α variation. When β is 0° or 15°, the influence of the embedded fracture has little effect on the failure strength and its anisotropy, in which the failure strength shows a decreasing trend over the entire α interval. As for β=30°, the failure strength is lower than that of intact shale. Under this condition, the variation trend of failure strength decreases from α=0° to α=45° and then remains roughly unchanged. For higher β of 45° ~ 90°, the failure strength is further lower than that when β is 30°. Here, increasing α makes the failure strength overall decline and fluctuate within a narrow range. Besides, it can be seen from Fig. 6b that when α remains constant, the failure strength decreases from β=0° to β=45° and increases from β=45° to β=90°, exhibiting a U-shaped distribution. This phenomenon suggests that a different α-β combination triggers a variable anisotropy of failure strength.

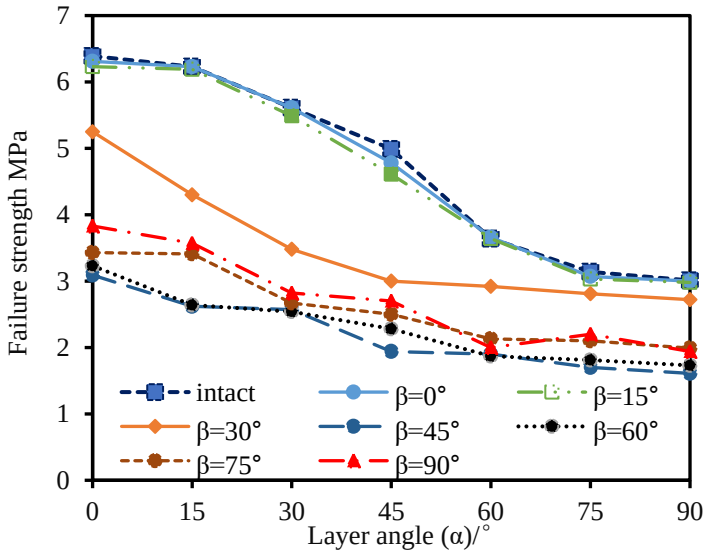

(a) failure strength among shales with different β value

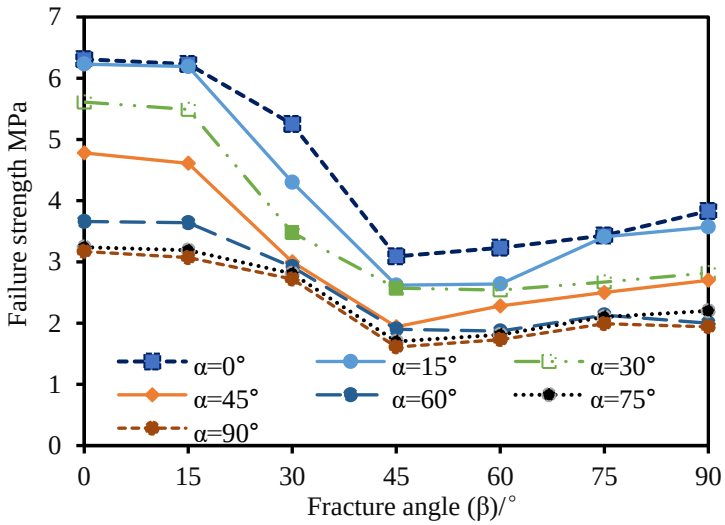

(b) failure strength among shales with different α value

Figure 6. Comparison of failure strengths among different shale models

3.2 Effect of α and β on the fracture pattern

In order to describe the fracture behaviour of shale under Brazilian tests, in this study, two kinds of fracture patterns are defined: original fracture (OF) represents that the generated main crack region is separated from the embedded fracture, while the induced fracture (IF) symbolizes that the development of the main crack results from the existence of the embedded fracture. The typical OF and IF types from numerical calculations are shown in Fig. 7, with the rest being tidied up in the Fig. S4 of SI. When β is 0° ~ 15°, the micro cracks occur through the sample and the main crack is mainly of the OF type, which is essentially consistent with the situation of intact shale. This phenomenon indicates that the existence of embedded fracture has little effect on shale failure (β=0°~15°), in terms of the entire α interval. This fracture pattern further explains why the failure strength value is the same as that of intact shale when β is relatively small (Fig. 6). When β increases to 30°, the effect of the embedded fracture on the fracture pattern becomes obvious. In this condition, the main crack is located between the loading point and the fracture tip, which is characterized as the IF type in the α range of 0° ~ 60°. Comparatively, the fracture pattern simultaneously comprises of OF and IF types for α of 75° or 90°. When β continues to increase (≥ 45°), the fracture pattern is regarded as IF for all α values. For the shale with an IF fracture pattern, its failure strength is lower than that of intact shale (Fig. 6). As far as the different α and β values, the fracture patterns are summarized in Fig. 8. It can be concluded that the effect of the embedded fracture on the failure behaviour tends to be noticeable when the fracture angle is high. Compared with the behaviour of intact shale, shale with prefabricated fracture always produces more secondary cracks (the cracks occur at the edges of the disks) during the failure process. These secondary cracks in the developing process show a common feature that they extend towards the tip of the embedded fracture (Fig. S4).

With regard to the damage of shale, there are four types of micro cracks, namely, matrix tension, matrix shear, layer tension and layer shear. As of the maximum load value, the proportion of different micro cracks changes with α variation complying with a similar tendency for different β value (taking β=15° as an example in Fig. 9). Generally, the matrix shear strength is higher than the strength of the other three types. The damage of samples during the loading process is mainly tensile (including matrix tension and layer tension), and the number of micro shear cracks is very small (Fig. 9). Moreover, the micro shear cracks in the matrix can even be ignored. With increasing α, layer damage is prone to occur, while the proportion of micro cracks in the matrix decreases. In addition, the proportion of cracks from layer shear (or layer tension) increases under the condition of higher α value (Fig. 9).

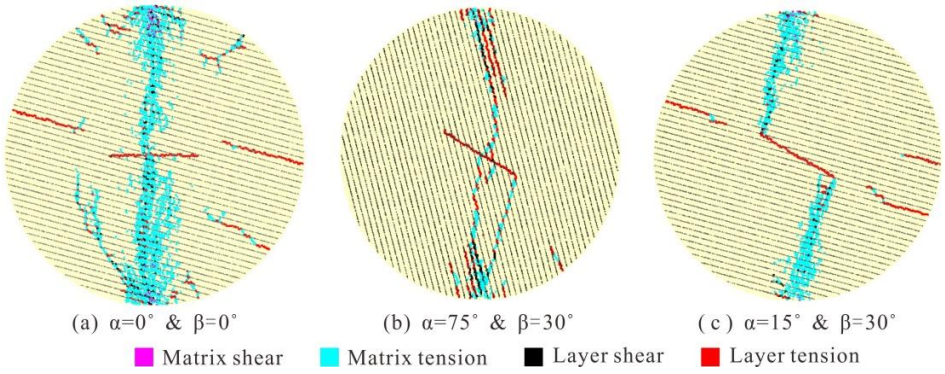

Figure 7. Representative of different fracture patterns in shale from numerical simulations. a, OF; b, OF & IF; c, IF.

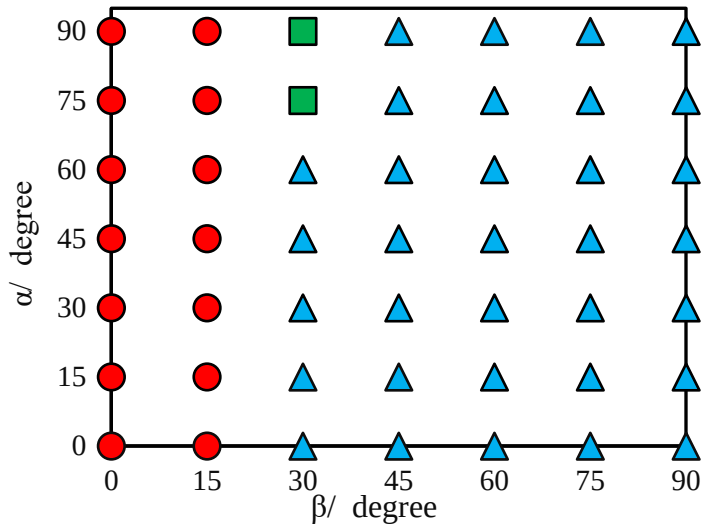

Figure 8. Summary of fracture patterns in shale from numerical simulations. (red circles represent OF, green squares represent the simultaneous existence of OF and IF, and blue triangles represent IF).

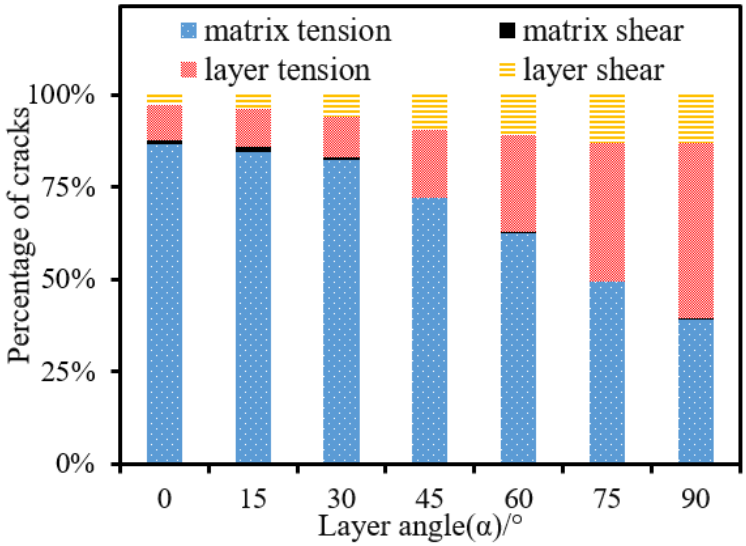

Figure 9. Micro cracks of shale with embedded fracture from numerical simulations under Brazilian tests (β=15°)

3.3 Evolution of micro cracks in shale with embedded fracture

The numerical simulations indicate the embedded fracture with a low β (0° or 15°) has a sparing effect on the evolution of micro cracks in shale. For example, the micro cracks in shale at β=0° (Figs. 10a-10c) develop in a way similar with that in intact shale (Fig. 5). This phenomenon results from that low β (0° or 15°) facilitates the OF failure mode (Fig. 8), where the embedded fracture seems inconsequential with the stimulated fracture. By contrast, the effect of the embedded fracture on the evolution of micro cracks in noticeable for greater β (30°~90°), where the fracture pattern can be regarded as IF type for almost all the samples (Fig. 9). The representative example (β=90°) in Figs. 10d-10f suggests there are only two types of evolution trends, namely, “incremental" type (e.g., α=45°) and "stepped" type (e.g., α is 0° or 90°). In

addition, Fig. 10 further indicates more shear cracks are generated at a lower β. As mentioned above, the fracture patterns and mechanisms determine the type of evolution of the micro cracks.

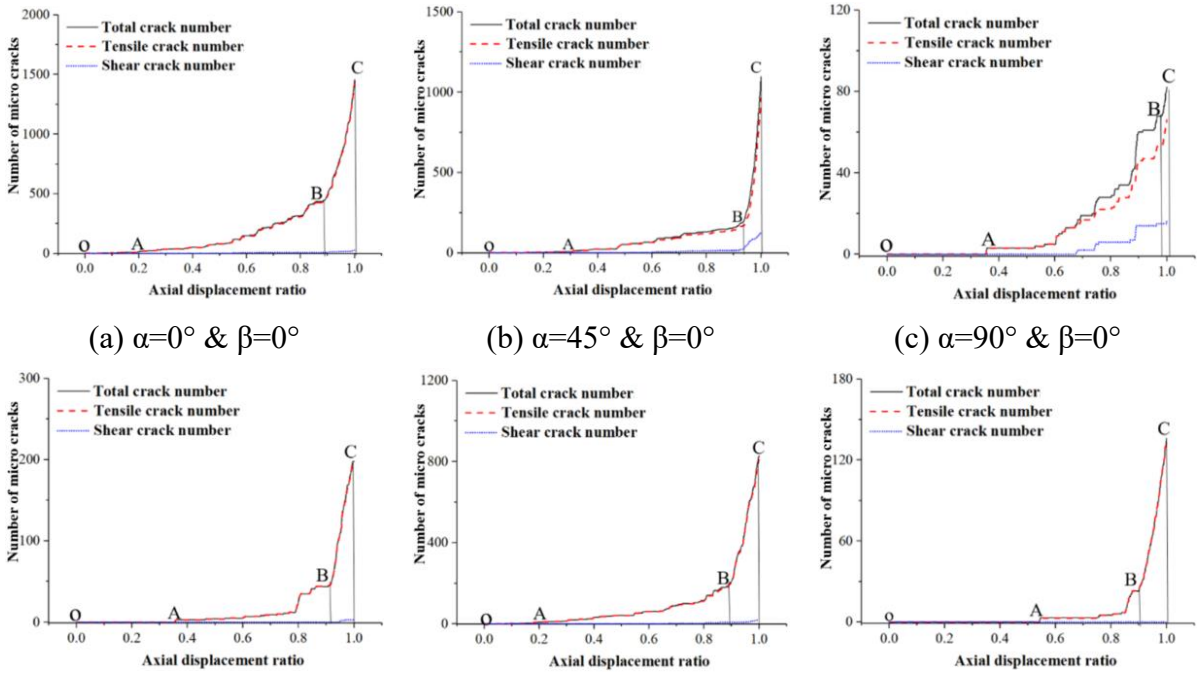

(a) α=0° & β=0° (b) α=45° & β=0° (c) α=90° & β=0°

(d) α=0° & β=90° (e) α=45° & β=90° (f) α=90° & β=90°

Figure 10. Evolution of micro cracks at variable α and β based on numerical simulations under Brazilian tests

4 Sensitivity analysis of layer strength parameters on shale failure

For layered shale reservoirs, the variable condition in sedimentation and diagenesis makes the mechanical properties of layer planes different (Geng et al., 2016; Feng et al., 2019). In this section, the sensitivity of layer SMJ strength on shale failure behaviour is explored based on two cases in Table 2 - Case 1 (Fixed csj & Variable σsj) and Case 2 (Variable csj & Fixed σsj). Case 1 (and Case 2) comprises of three models and is set for sensitivity investigation of tensile (and cohesion) strength on shale failure behaviour. In two cases, the ratio of base value to the variables is 0.5, 1.0 and 1.5, in which the base values (σsj = 4 MPa, csj = 15 MPa) are referred from Table 1. Besides, other parameters in the numerical models remain unchanged (Table1).

Table 2. Settings parameters for sensitivity analysis of layer strength

Case 1: Fixed csj & Variable σsj				**Case 2**: Variable csj & Fixed σsj			
csj (MPa)	15	15	15	csj (MPa)	7.5	15	22.5
σsj (MPa)	2	4	6	σsj (MPa)	4	4	4
Series	LT model	MT model	HT model	Series	LS model	MS model	HS model

Note: csj is the SJM cohesion strength, while σsj represents SJM tensile strength.

4.1 Sensitivity of the SMJ tensile strength on shale failure (Case 1)

In Case 1, four α values and three β values are discussed in each model. The failure strength curves suggest that increasing α makes the failure strength of all samples decrease no matter what the β is, except the situation of α=90° and β=90° (Fig. 11). The fracture pattern and

mechanism indicate that a higher layer tensile strength induces fewer secondary cracks in the model (Figs. S5-S7). Moreover, for all β scope, when α is low (0° or 30°), the failure behaviour of shale in all series of Case 1 is regarded as the same (Figs. S5-S7), suggesting the variation of tensile strength is not sensitive to the shale failure at low α. However, with increasing α, the failure mechanisms are different among models.

4.1.1 Situation of β=0°

For β equals 0°, the fracture pattern of each model is OF type. As for three models, the failure mechanism is dominated by matrix tensile failure when α is 0°, and the effect of the variation in SMJ tensile strength on the failure strength is negligible at α=0° but becomes obvious as α increases (Fig. 11a). For the LT model, when α is 30° or 60°, many layer tensile cracks occur near the loading points. Moreover, a macroscopic tensile failure plane has formed at α=60°, which leads to a lower failure strength than that of the other two groups (Fig. 11a). When α is 90°, the failure of the LT model and the HT model is induced by the layer tension cracks and the layer shear cracks, respectively (Fig. S5). With regard to the MT model, the layer tension cracks occur near the loading points, and the layer shear cracks occur in the middle of the disk. Hence, different failure mechanisms give rise to different failure strengths.

4.1.2 Situation of β=45°

In this operation conditions, all the fracture patterns of the samples are IF type. Compared with the results of the MT model, the failure strength of the LT model decreases, while that of the HT model remains unchanged at α=0° (Fig. 11b). When α is 0°~60°, the matrix tension cracks play a major role in the main damage region, where more layer shear cracks occur with increasing SMJ tension strength (Fig. S6).

It should be noted that when α is 90°, the failure mechanisms are obviously different for the three models. Because the SMJ tension strength is very low in the LT model, the damage mainly develops along the layer plane from the embedded fracture tip and then towards the loading point. In addition, some layer tension cracks also occur in the middle of the disk. Comparatively, with increasing SMJ tension strength, the number of layer tension cracks decreases. For the MT model, the main damage region is composed of matrix tension cracks, layer tension cracks and layer shear cracks. However, with regard to the HT model, the layer tension cracks have not occurred, while the layer shear cracks and the matrix tension cracks determine the failure mechanism and the failure strength (Fig. S6).

4.1.3 Situation of β=90°

Basically, the fracture pattern is regarded as IF type for all models at β=90°(Fig. S7). For the situation of α=0°, the failure strength of three models are the same, suggesting the influence of the SMJ tension strength on the failure mechanism of each model can be treated identically (Fig. 11c). However, as α increases, the failure strength of LS model and MS model declines continuously, by contrast, while that of the HT model decreases first and then increases with the minimum value at α=60°. This variation mainly depends on the relative magnitude of the critical failure strength of different cracks. In addition, under the conditions of β=90° and β=45°, the SMJ tension strength has a similar influence on the damage mechanism and stimulates IF type fractures, compared with the situation of β=0° (OF type fractures).

Based on the analysis above, the failure strength of shale is related to the tensile strength of layer planes, but its correlation degree is affected by the directions of the layer and embedded fracture (namely, α and β). The failure strength can also be reflected in the fracture pattern and failure mechanism - a greater number of shear cracks corresponds a higher failure strength, referring to the same failure modes.

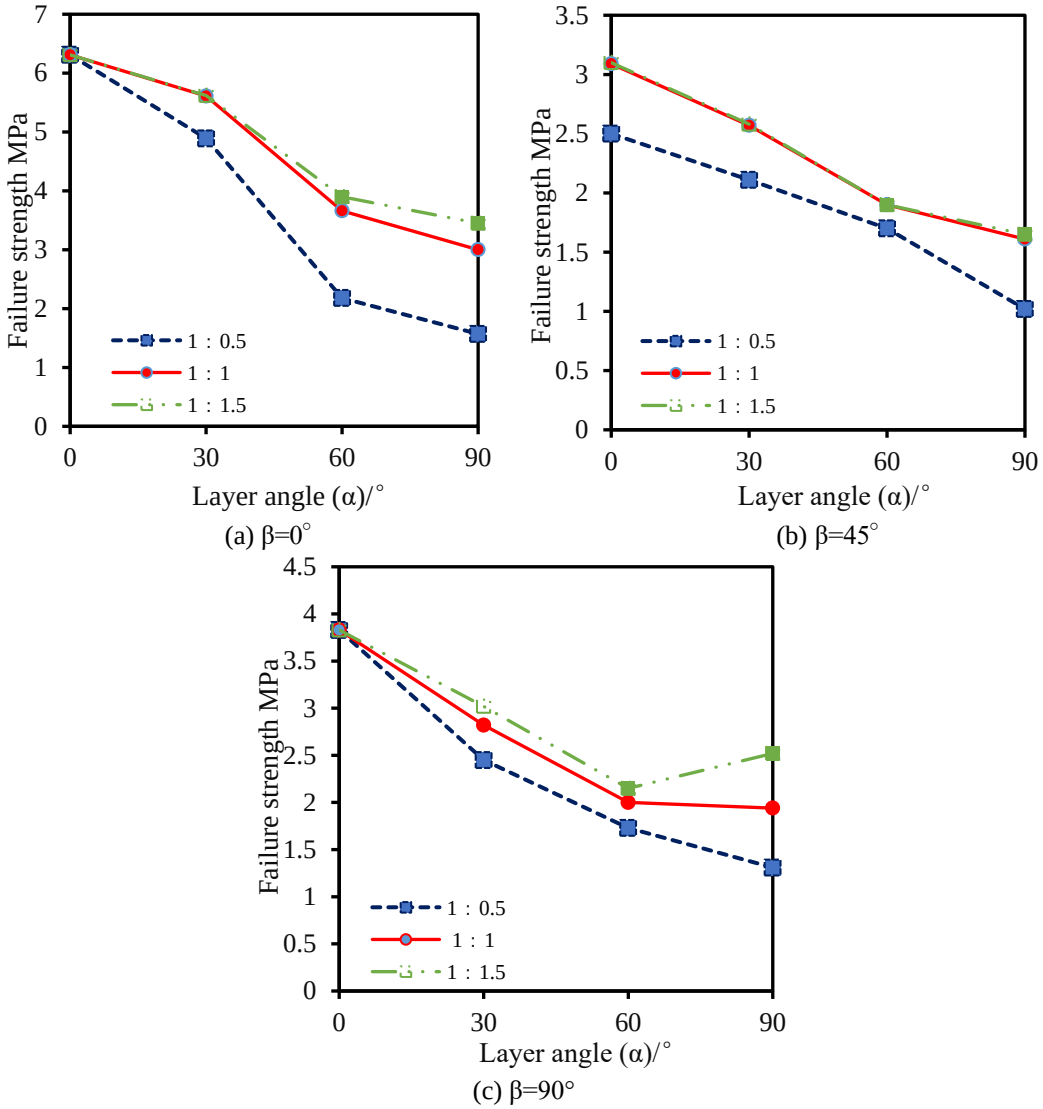

Figure 11. Effect of SMJ tensile strength on the failure strength of shale based on numerical simulations (1:0.5, LT model; 1:1, MT model; 1:1.5, HT model)

4.2 Sensitivity of SMJ cohesion strength on shale failure (Case 2)

In Case 2, the α and β values adopted in Case 1 are also discussed in each model. As for all models in Case 2, increasing α diminishes the failure strength of shale with different β values (Fig. 12). The numerical investigations also reveal that fewer secondary cracks tend to emerge in the model with higher cohesion strength (HS model) than the one with lower cohesion strength (LS model) (Figs. S8-S10). The details about the influence of cohesion strength variation on shale failure behaviour are exhibited as below.

4.2.1 Situation of β=0°

According to the failure strength curves, the failure strength is the same at α=0° and declines gradually with increasing α, among which the decrement of failure strength for LS model is obviously greater than that for HS model (Fig. 12a). For the fracture pattern, it is similar for all three models with a OF type. When α is 0°, the damage zone is located in the middle of three models and the main cracks are of the matrix tension type (Fig. S8). Nevertheless, the secondary cracks come from layer shear at lower cohesive strength (LS model), while those are basically from layer tension in HS model at α=0°. When α increases to 30° and 60°, the lower cohesive strength (LS model) controls the damage that develops alone the layer planes, where the damage zone deviates from the middle of LS model. Comparatively, the damage zone of the MS and HS models is closer to the model centre than that of LS model (Fig. S8). Moreover, fracture patterns of three models suggest a higher layer cohesive strength induces fewer layer shear cracks but more layer tension cracks, at α=30° or 60°. When α is 90°, the failure in the LS model and HS model is induced by the layer shear cracks and the layer tension cracks, respectively. For the MS model, the layer tension cracks occur in the middle of the disk, while the layer shear cracks occur near the loading points at α=90°.

4.2.2 Situation of β=45°

In this situation, all the fracture patterns of all models are IF type (Fig. S9). For all α values, there is hardly any layer tension cracking with regard to the LS model, by contrast, while more layer tension cracks tend to occur than layer shear cracks in the MS model and HS model (Fig. S9). In particular, when α is 0°, the failure mechanism is mainly matrix tension for HS model, which leads to a much higher failure strength than that of other two models (LS and MS models). When α increases to 30° and 60°, the variation of cohesion strength has limited influence on the shale failure behaviour, revealed by the failure strength and fracture patterns (Fig. 12b and Fig. S9). When α is 90°, the damage develops along the layer plane from the natural fracture tip. The difference at α=90° is that layer shear cracks occur in the LS model, whereas layer tension cracks occur in the MS model and HS mode.

4.2.3 Situation of β=90°

The variation tendency of failure strength in this situation is similar with that when β is 90°, that is, increasing α is able to diminish the failure strength and the decrement of failure strength for LS model is greater than that for HS model (Fig. 12c). In terms of the fracture pattern, IF type fracture emerges in all models and the main damage region is located in the middle of the models (Fig. S10). Similar with the phenomenon at β=0° or 45°, the secondary cracks mainly come from layer shear in LS model and are mainly from layer tension in MS and HS models at β=90° (Fig. S10). From α=0° to α=90°, fractures originated from matrix tension occupies a decreasing proportion. Besides, for all α values, the main damage zone is in the middle of all models.

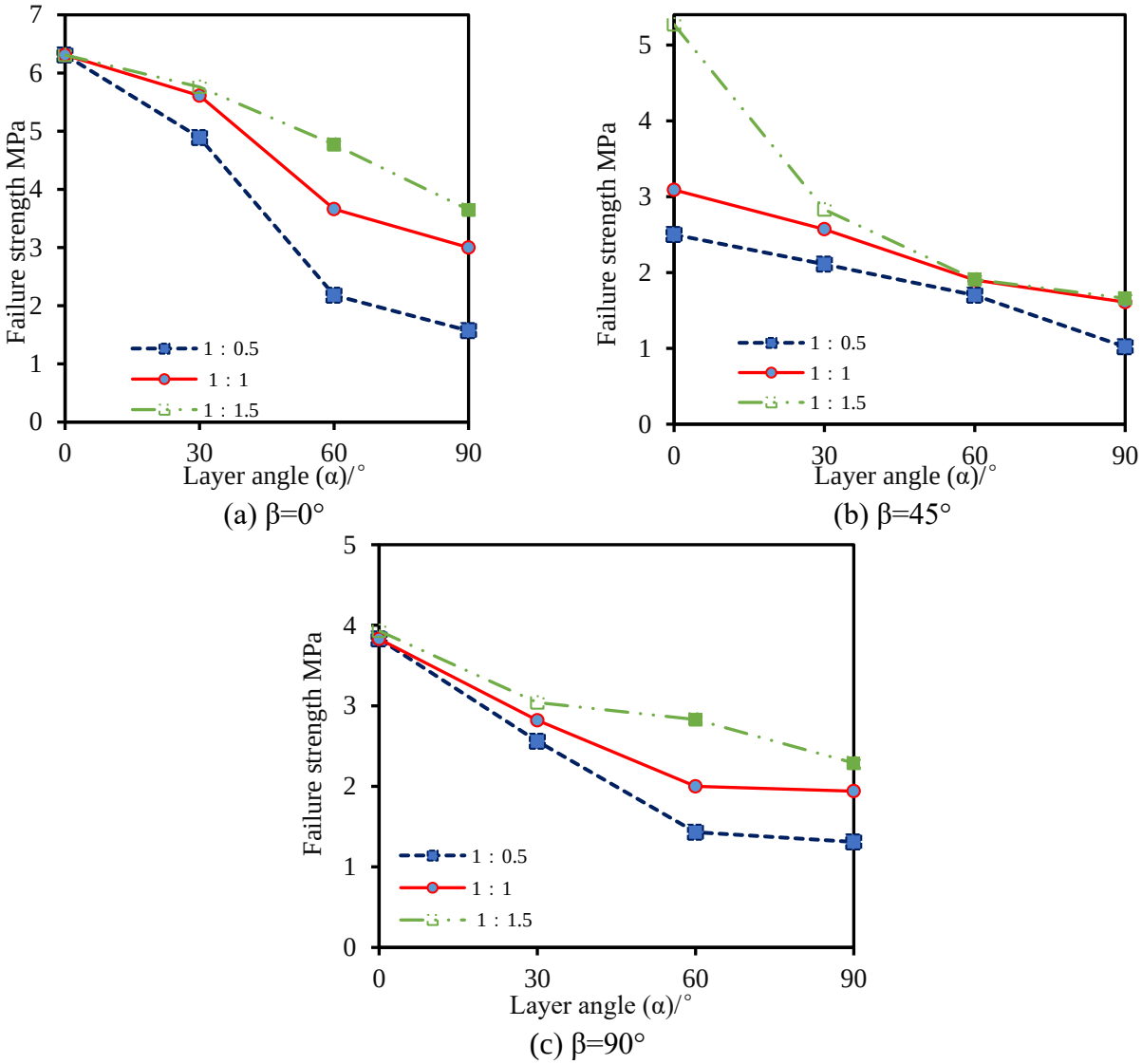

Figure 12. Effect of SMJ cohesion strength on the failure strength based on numerical simulations (1:0.5, LS model; 1:1, MS model; 1:1.5, HS model)

4.3 Discussion on the layer strength parameters

Based on the numerical results discussed above, the fracture pattern of the models tends to be OF type when α is 0°, suggesting the existence of embedded fracture does not affect the fracture pattern. When β increases to 45° or 90°, the influence of the embedded fracture obviously affects the fracture pattern that is regarded as IF type. In addition, if β and the layer strength remain constant, increasing α renders the layer planes more easily damaged, and the failure strength shows a decreasing trend. Besides, higher layer strength normally increases the failure strength. However, the variation in the failure strength depends on the damage mechanism. When α is 0° and β is 0° or 90°, the matrix tension cracks dominate the failure process, and the layer strength has little effect on the failure strength of the models.

With regard to the failure of the layer plane, the damage can occur under tension or shear failure, which is determined by the relative magnitude of the layer tension strength and the

cohesive strength. For example, when α and β are both 90°, although the damage region is in a straight-line shape, the failure mechanism is different. In contrast to the behaviour of the M (MT or MS) model, a higher layer tension strength (or layer cohesion) leads to layer shear damage (or layer tension damage). Certainly, the failure strength is also different.

5 Conclusion

This paper establishes a numerical model in PFC2D to investigate the failure mechanism of shale containing natural fracture under Brazilian tests, which yields the following conclusions:

(1) The failure strength and fracture pattern of shale embedded with fracture is jointly determined by α and β. For different β, the failure strength curves can be divided into three types with the variation in α. The presence of fractures reduces the anisotropy of the shale failure strength. Numerical results further indicate that the fracture pattern is dominated by IF at lower β (< 30°), while that is dominated by OF at β > 30°.

(2) The absorption energy curve of intact shale grows nonlinearly, where a lower α enables the sample absorb more energy. Under the conditions of different α, the micro cracks in intact shale exhibits three evaluation modes, namely, “incremental” mode, “smooth” mode and “stepped” mode. By comparison, as for the micro cracks in shale containing natural fracture, there are only two evolution trends: the “incremental" type at α=0°~30° and the "stepped" type for higher α.

(3) The influence from the variation of layer strength parameters on the fracture pattern is negligible at β=0° and becomes obvious if β>0°. If β and layer strength remain constant, the failure strength decreases with increasing α. Moreover, growing layer strength normally increases the failure strength (except when the damage mode is dominated by matrix). As for different shale models, although the failure pattern (OF or IF) may stay same, the failure mechanism is likely to be different, thus imparting different failure strengths.

Acknowledgements

This study is funded by the National Natural Science Foundation of China (No. 51704197, No. 11872258) and the Open Fund from the Key Laboratory of Deep Underground Science and Engineering (No. DUSE201804). The authors would like to thank Mr. Bo He from Institute of New Energy and Low-Carbon Technology of Sichuan University for his help with experimental operations of Brazilian tests. The data archiving is underway using Mendeley Data repository, so please see data in Supporting Information for review purposes.

References

Alm, O., Jaktlund, L. L., and S. Q. Kuo (1985), The influence of microcrack density on the elastic and fracture mechanical properties of Stripa granite. *Phys. Earth Planet. In.,* 40(3), 0-179.

Al-Maamori, H. M. S., El Naggar, M. H., and S. Micic (2019), Wetting effects and strength degradation of swelling shale evaluated from multistage triaxial test. *Undergr. Sp.*, 4(2), 79-97.

Arora, S., and B. Mishra (2015), Investigation of the failure mode of shale rocks in biaxial and triaxial compression tests. *Int. J. Rock Mech. Min.,* 79, 109-123.

494 Bennett, K. C., Berla, L. A., Nix, W. D., and R. I. Borja (2015), Instrumented nanoindentation
495 and 3D mechanistic modeling of a shale at multiple scales. *Acta Geotech.*, 10(1), 1-14.
496 Cai, M. (2013), Fracture Initiation and Propagation in a Brazilian Disc with a Plane Interface: a
497 Numerical Study. *Rock Mech. Rock Eng.*, 46(2), 289-302.
498 Chong, Z. H., Li, X. V. H., Hou, P., Wu, Y. C., Zhang, J., Chen, T., and S. Liang (2017),
499 Numerical investigation of bedding plane parameters of transversely isotropic shale. *Rock*
500 *Mech. Rock Eng.*, 2017, 50(5), 1183-1204.
501 Ding, X., Zhang, L., Zhu, H., and Q. Zhang (2014), Effect of model scale and particle size
502 distribution on PFC3D simulation results. *Rock Mech. Rock Eng.*, 2014, 47(6), 2139-2156.
503 Dou, F., Wang, J. G., Zhang, X., and H. Wang (2019), Effect of joint parameters on fracturing
504 behavior of shale in notched three-point-bending test based on discrete element model. *Eng.*
505 *Fract. Mech.*, 205, 40-56.
506 Feng, G., Kang, Y., Sun Z. D., Wang, X. c., and Y. Q. Hu (2019), Effects of Supercritical CO_2
507 adsorption on the mechanical characteristics and failure mechanisms of shale. *Energy*, 173,
508 870-882.
509 Gao, F., Stead, D., and D.Elmo (2016), Numerical simulation of microstructure of brittle rock
510 using a grain-breakable distinct element grain-based model. *Comput. Geotech.*, 2016, 78,
511 203-217.
512 Geng, Z., Chen, M., Jin, Y., Yang, S., Yi, Z. C., Fang, X., and X. Y. Du (2016), Experimental
513 study of brittleness anisotropy of shale in triaxial compression. *J. Nat. Gas Sci. Eng.*, 36,
514 510-518.
515 Haeri, H., Shahriar, K., Marji, M. F., and P. Moarefvand (2014), Experimental and numerical
516 study of crack propagation and coalescence in pre-cracked rock-like disks. *Int. J. Rock*
517 *Mech. Min.*, 67, 20-28.
518 He, J., and L. O. Afolagboye (2018), Influence of layer orientation and interlayer bonding force
519 on the mechanical behavior of shale under Brazilian test conditions. *Acta Mech. Sinica-Prc.*,
520 34(2), 349-358.
521 Heng, S., Guo, Y. T., Yang, C. H., Daemen, J. J. K., and Z. Li (2015), Experimental and
522 theoretical study of the anisotropic properties of shale. *Int. J. Rock Mech. Min.*, 74(1), 58-
523 68.
524 Jia, L. C., Chen, M., Jin, Y., and H. L. Jiang (2017), Numerical simulation of failure mechanism
525 of horizontal borehole in transversely isotropic shale gas reservoirs. *J. Nat. Gas Sci. Eng.*,
526 45, 65-74.
527 Li, C., Ostadhassan, M., Guo, S., Gentzis, T, and L. Kong (2018), Application of PeakForce
528 tapping mode of atomic force microscope to characterize nanomechanical properties of
529 organic matter of the Bakken Shale. *Fuel*, 233, 894-910.
530 Liu, J., Yao, Y. B., Elsworth, D., Liu, D. M., Cai, Y. D., and L. Dong L (2017), Vertical
531 heterogeneity of the shale reservoir in the lower silurian longmaxi formation: analogy
532 between the southeastern and northeastern Sichuan basin, SW China. *Minerals*, 7(8), 151.
533 Liu, J., Yao, Y. B., Elsworth, D., Pan, Z. J., Sun, X. X., and W. H. Ao (2016), Sedimentary
534 characteristics of the Lower Cambrian Niutitang shale in the southeast margin of Sichuan
535 Basin, China. *J. Nat. Gas Sci. Eng.*, 36, 1140-1150.
536 Luo, Y., Xie, H. P., Ren, L., Zhang, R., Li, C. B., and C. Gao (2018), Linear Elastic Fracture
537 Mechanics Characterization of an Anisotropic Shale. *Sci. Rep.*, 8(1), 8505.

538 März, C., Poulton, S. W., Beckmann, B., Küster, K.,Wagner, T., and S. Kastend (2008), Redox
539 sensitivity of P cycling during marine black shale formation: dynamics of sulfidic and
540 anoxic, non-sulfidic bottom waters. *Geochim. Cosmochim. Ac.*, 72(15), 3703-3717.
541 Mohtar, R. H., Shafiezadeh, H., Blake, J., and B. Daher (2019), Economic, social, and
542 environmental evaluation of energy development in the Eagle Ford shale play. *Sci. Total*
543 *Environ.,* 646, 1601-1614.
544 Na, S. H., Sun, W. C., Ingraham, M. D. and H. K. Yoon (2017), Effects of spatial heterogeneity
545 and material anisotropy on the fracture pattern and macroscopic effective toughness of
546 Mancos Shale in Brazilian tests. *J. Geophys. Res-Sol.* Ea., 122(8), 6202-6230
547 Nezhad, M. M., Fisher, Q. J., Gironacci, E., and M. Rezania (2018), Experimental Study and
548 Numerical Modeling of Fracture Propagation in Shale Rocks During Brazilian Disk Test.
549 *Rock Mech. Rock Eng.,* 51(6), 1755-1775.
550 Park. B., and K. B. Min (2015), Bonded-particle discrete element modeling of mechanical
551 behavior of transversely isotropic rock. *Int. J. Rock Mech. Min.,* 76, 243-255.
552 Planas, J., Guinea, G. V., and M. Elices (1999), Size effect and inverse analysis in concrete
553 fracture. *Int. J. Fracture,* 95(1-4), 367-378.
554 Shi, X. S., Yao, W., Liu, D., Xia, K., Tang, T., and Y. Shi (2019), Experimental study of the
555 dynamic fracture toughness of anisotropic black shale using notched semi-circular bend
556 specimens. *Eng. Fract. Mech.,* 205, 136-151.
557 Tan, X., Konietzky, H., Frühwirt, T., and D. Q. Dan (2015), Brazilian tests on transversely
558 isotropic rocks: laboratory testing and numerical simulations. *Rock Mech. Rock Eng.,* 48(4),
559 1341-1351.
560 Vervoort, A., Min, K. B., Konietzky, H., Cho, J. W., Debecker, B., Dinh, Q. D., Frühwirt, T.,
561 and A. Tavallali (2014), Failure of transversely isotropic rock under Brazilian test
562 conditions. *Int. J. Rock Mech. Min.,* 70, 343-352.
563 Wang, P., Cai, M., and F. Ren (2018), Anisotropy and directionality of tensile behaviours of a
564 jointed rock mass subjected to numerical Brazilian tests. *Tunn. Undergr. Sp. Tech*., 73, 139-
565 153.
566 Wang, Z., Jacobs, F., and M. Ziegler M (2014), Visualization of load transfer behaviour between
567 geogrid and sand using PFC2D. *Geotext. Geomembranes,* 2014, 42(2), 83-90.
568 Wanniarachchi, W. A. M., Ranjith, P. G., Perera, M. S. A., Rathnaweera, T. D., Zhang, D. C.,
569 and C. Zhang (2018), Investigation of effects of fracturing fluid on hydraulic fracturing and
570 fracture permeability of reservoir rocks: An experimental study using water and foam
571 fracturing. *Eng. Fract. Mech.*, 194, 117-135.
572 Wu, S., Ma, J., Cheng, Y., Xu, M., and X. Huang (2018), Numerical analysis of the flattened
573 Brazilian test: Failure process, recommended geometric parameters and loading conditions.
574 *Eng. Fract. Mech.*, 204, 288-305.
575 Xu, G., He, C., Chen, Z., and D. Wu (2018), Effects of the micro-structure and micro-parameters
576 on the mechanical behaviour of transversely isotropic rock in Brazilian tests. *Acta Geotech.,*
577 13, 887–910.
578 Yang, S. Q., and Y. H. Huang (2014), Particle flow study on strength and meso-mechanism of
579 Brazilian splitting test for jointed rock mass. *Acta Mech. Sinica-Prc.*, 2014, 30(4), 547-558.
580 Yang, Z. P., He, B., Xie, L. Z., Li, C. B., and J. Wang (2015), Strength and failure modes of
581 shale based on Brazilian test. *Rock Soil. Mech.,* 36(12), 3447-3455.

Yin, H., Zhou, J. P., Xian, X. F., Jiang, Y. D., Lu, Z. H., Tan, J. Q., and G. J. Liu (2017), Experimental study of the effects of sub- and super-critical CO_2 saturation on the mechanical characteristics of organic-rich shales. Energy, 132, 84-95.

Zeng. X., and Y. Wei (2016), The influence of crack-orientation distribution on the mechanical properties of pre-cracked brittle media. *Int. J. Solids Struct.*, 96, 64-73.

Zhang, L., Zhou, J., Braun, A., and Z. Han (2018), Sensitivity analysis on the interaction between hydraulic and natural fractures based on an explicitly coupled hydro-geomechanical model in PFC2D. *J. Petrol. Sci. Eng.*, 167, 638-653.

Zhang, S. W., Shou, K. J., Xian, X. F., Ping, Z. J., and G. J. Liu (2018), Fractal characteristics and acoustic emission of anisotropic shale in Brazilian tests. *Tunn. Undergr. Sp. Tech.*, 71, 298-308.

Zhang, S. W., Shou, K. J., Xian, X. F., Zhou, J. P., and G. J. Liu (2018), Fractal characteristics and acoustic emission of anisotropic shale in Brazilian tests. *Tunn. Undergr. Sp. Tech.*, 71, 298-308.

Zhang, Y., Li, T., Xie, L.,Yang, Z., and R. Li (2017),. Shale lamina thickness study based on micro-scale image processing of thin sections. *J. Nat. Gas Sci. Eng.*, 46, 817-829.

Zhang, Z., Wang, L., Wang, Y., and X. Chu (2019), Discrete element simulation on mixing of granular materials in rotated container. *Eng. Anal. Bound. Elem.*, 106, 20-26.

Zhao Z. H., and H. P. Xie (2008), Energy Transfer and Dissipation in Rock Deformation and Failure Process. *J. Sichuan Univ. (Eng. Sci.)*, 40(2), 26-31.

Zhou, J., Zhang, L. Q., Pan, Z. J., and Z. H. Han (2016), Numerical investigation of fluid-driven near-borehole fracture propagation in laminated reservoir rock using PFC2D[J]. *J. Nat. Gas Sci. Eng.*, 36(Part A), 719-733.

Zhou, J., Zhang, L. Q., Pan, Z. J., and Z. H. Han (2017), Numerical studies of interactions between hydraulic and natural fractures by Smooth Joint Model. *J. Nat. Gas Sci. Eng.*, 2017, 46, 592-60.

Zhou, J. P., Tian, S. F., Zhou, L., Xian, X. F., Yang, K., Jiang, Y. D., Zhang, C. P., and Y. W. Guo (2019), Experimental investigation on the influence of sub- and super-critical CO2 saturation time on the permeability of fractured shale. *Energy*, 18, 116574.

Zhou, X. P., and Y. T. Wang (2016), Numerical simulation of crack propagation and coalescence in pre-cracked rock-like Brazilian disks using the non-ordinary state-based peridynamics. *Int. J. Rock Mech. Min.*, 89, 235-249.